

Resonant Raman scattering off neutral quantum dots

Alain Delgado^{a1}, Augusto Gonzalez^{b2}, and Eduardo Menéndez-Proupin^{c3}

¹*Centro de Estudios Aplicados al Desarrollo Nuclear, Ciudad Habana, Cuba*

²*Instituto de Cibernética, Matemática y Física, Calle E 309, Vedado, Habana 4, Cuba*

³*Instituto de Materiales y Reactivos, Universidad de La Habana, Cuba*

(Received: November 6, 2018)

Abstract

Resonant inelastic (Raman) light scattering off neutral GaAs quantum dots which contain a mean number, $N = 42$, of electron-hole pairs is computed. We find Raman amplitudes corresponding to strongly collective final states (charge-density excitations) of similar magnitude as the amplitudes related to weakly collective or single-particle excitations. As a function of the incident laser frequency or the magnetic field, they are rapidly varying amplitudes. It is argued that strong Raman peaks should come out in the spin-density channels, not related to valence-band mixing effects in the intermediate states.

PACS: 78.30.-j, 78.67.Hc

Keywords: Raman scattering, quantum dots, electron-hole systems

I. INTRODUCTION

The experimental study of the inelastic (Raman) scattering of light in arrays of quantum dots (qdots) began a few years ago^{1,2}. These studies were aimed at investigating multipole excitations or spin excited states in the quantum dot, which do not leave traces in luminescence or absorption experiments. In both papers, quasi-bidimensional dots with radii around 100 nm and nominal electron density about $8 \times 10^{11} \text{ cm}^{-2}$ were studied. A rich spectrum of single-particle (SPE), and collective charge-density (CDE) and spin-density excitations (SDE) was observed.

The single-particle spectra were interpreted in terms of the single-particle density of states in the dot¹, computed in the Hartree-Fock (HF) approximation. The energy position and Raman strengths of CDE states in dots with 12 electrons, computed within time-dependent HF theory³, were shown to qualitatively agree with the experimental results. More consistent calculations in the framework of time-dependent density-functional theory (DFT) were carried out in Ref. 4, where the charge and spin dynamic structure functions were computed for a system of 200 electrons. The multipolarities of the observed CDE and SDE peaks, and the relative peak intensities, as functions of the transferred wave vector of the light, were reproduced.

Let us stress that, in electron qdots, Raman processes in which the final states are SDE require the account for valence-band mixing in the intermediate hole state. For this reason, CDE peak intensities reported in Ref. 4 can not be properly compared with intensities in the SDE channels. The inclusion of valence-band mixing effects in the intermediate states of Raman processes is to be published elsewhere⁵.

In the present paper, we compute Raman amplitudes for neutral quantum dots, where the number of holes, N , equals the number of electrons in the dot. To the best of our knowledge, there are no similar calculations in the literature.

Although the lifetime of the excitons may pose certain difficulties to the Raman measurements, we believe that it does not represent a real challenge to present experiments. With relative independence on the dot parameters, the multi-excitonic system reaches typical densities around $5 \times 10^{11} \text{ pairs/cm}^2$, a value which may be obtained by pumping a neutral qdot with a stationary mean-power laser. In fact, densities well above 10^{12} cm^{-2} have been achieved already for a few years⁶ with pulsed high-power lasers.

Due to the lack of experimental results, we will focus on the qualitative aspects following from our calculations. A simplified two-band model of a disk-shaped qdot with parabolic confinement⁷ is to be used.

We shall, first, make some remarks concerning the computational method. The Random Phase Approximation (RPA) is the common frame, as in the cited papers. We adopt the wave-function approach of Nuclear Physics⁸, and construct RPA approximations to the wave functions of both final and intermediate states. Coulomb interactions and collective effects are exactly accounted for within the RPA, even for the intermediate states entering the Raman amplitudes, which are states with $N + 1$ e-h pairs. Corrections to the RPA functions, such as the e-h pairing correlations, could, in principle, be included by means of the quasiparticle RPA scheme⁸. The electron-radiation (e-r) interaction hamiltonian is

written in second quantization in the basis of HF single-particle states. Our treatment of Raman scattering follows the lines of Refs. 9 and 10, in the sense that the e-r interaction causes transitions between multi-excitonic states. Thus, energy denominators contain N -pair instead of single-particle energies.

Concerning the numerical results, there are a few points to stress. First, the absorption threshold, or the frequency for which extreme resonance is achieved in Raman scattering, grows at a rate of 0.3 meV per pair added to the dot. This is an indirect way of determining the mean number of pairs in the dot. Second, Raman peaks in quadrupole channels are 1/10 of monopole peaks at momentum transfer around $0.8 \times 10^5 \text{ cm}^{-1}$. Next, intensities corresponding to weakly collective or SPE are comparable in magnitude to the strongest CDE peaks, and vary very rapidly with the magnetic field or the frequency of the incident laser. Thus, our calculated spectra resemble more the complex spectra of quantum wells in strong magnetic fields¹¹, and differ from the smooth experimental curves obtained in Ref. 2 for the pure electronic strong-confinement qdot.

A last point which deserves attention is the fact that Raman scattering in SDE channels do not require mixing of hole bands. Thus SDE peaks should be observed in any polarization of the scattered light.

The present calculation of Raman cross sections completes a series of papers on the optical properties of the N -pair system in a qdot. The dominance of a giant dipole resonance in the infrared absorption, which position scales as $N^{1/4}$, was shown in Ref. 12. This resonance could be studied through the modulations of the photoluminescence caused by an infrared source, in the same way as the infrared excitations in the “ N -electron plus one hole” system are presently studied¹³. On the other hand, the position and intensity of the coherent magneto-luminescence peak were computed in Ref. 14.

The plan of the paper is as follows. The basic expressions for Raman cross sections along with HF, RPA and particle-particle Tamm-Dancoff approximations (pp-TDA) are presented in Section II. The formalism is well established in the Nuclear Physics context⁸. We underline in that section only the main points for the sake of completeness. Computed ground-state properties, the multipole excitations and their strength variations with magnetic field, the band gap renormalization as a function of the number of pairs, and the Raman cross sections are given in Section III. Final remarks are presented at the end.

II. THE BASICS

The resonant inelastic (Raman) light scattering off a neutral quantum dot containing a mean number, N , of electron-hole pairs is schematically represented in Fig. 1. The energy of the incident photon, $\hbar\omega_i$, is supposed to be close to the band gap energy, E_{gap} . In Fig. 1 (a), the final state has the same spin quantum numbers as the initial (ground) state of the N -pair system. It is, in general, a charge-density excitation (CDE). The electron and hole spins are represented by arrows. Incident and emitted photons are drawn as wavy lines. Additionally, there are also Raman processes in which the final states involve changes in the spin quantum numbers. These states will be called spin-density excitations (SDE). We have represented in Fig. 1 (b) a situation in which the total electron and total hole spin projections experience changes $\Delta S_{ze} = -1$ and $\Delta S_{zh} = +1$, respectively.

The amplitude for the Raman processes depicted in Fig. 1 (a) is given by:

$$A_{fi}^{CDE} = \sum_{int} \frac{\sqrt{N_f + 1} {}_N\langle f | H_{e-r}^+ | int \rangle_{N+1} {}_{N+1}\langle int | H_{e-r}^- | i \rangle_N \sqrt{N_i}}{\hbar\omega_i - (E_{int} - E_i) + i\Gamma}, \quad (1)$$

where N_i , N_f are the mean number of photons in the initial and final states. For spontaneous Raman scattering, $N_f = 0$. The sum runs over intermediate states with $N + 1$ pairs and the appropriate quantum numbers. Γ is the lifetime broadening. We will take it phenomenologically as $\Gamma = 0.5$ meV.³ The resonance condition means that the leading contribution to (1) comes from intermediate states satisfying

$$\hbar\omega_i \approx E_{int} - E_i, \quad (2)$$

i. e. the incident photon has nearly the same energy as the jump in energy from the initial to the intermediate quantum-dot state.

H_{e-r}^- is the interaction hamiltonian corresponding to the annihilation of a photon and creation of a new electron-hole pair. Its matrix element is written as

$${}_{N+1}\langle int | H_{e-r}^- | i \rangle_N = \frac{e}{m_0} \sqrt{\frac{2\pi\hbar}{V\omega_i\eta_i^2}} \sum_{\alpha,\gamma} (\vec{\varepsilon}_i \cdot \vec{p}_{\alpha\gamma}) \left(\int e^{i\vec{q}_i \cdot \vec{r}} \phi_{\alpha e}^*(\vec{r}) \phi_{\gamma h}^*(\vec{r}) d^3r \right) \times {}_{N+1}\langle int | e_\alpha^\dagger h_\gamma^\dagger | i \rangle_N. \quad (3)$$

In the normalization factor entering Eq. (3), e is the electron charge, m_0 is the electron mass in vacuum, V is the sample volume, and η_i is the refraction index at frequency ω_i . On the other hand, the first factor in the sum comes from the (band) spin quantum numbers of the initial and final states in the interband transition. We give its detailed expression in Appendix A. $\vec{\varepsilon}_i$ is the polarization vector of the incident light.

The next factor in the sum depends on the orbital (envelope) one-particle wave functions. As a basis for the one-particle states, we will use the Hartree-Fock (HF) set, $\phi_{\alpha e}$ and $\phi_{\gamma h}$ for electrons and holes respectively. \vec{q}_i is the wave vector of the incident light. Detailed expressions for the orbital factor are given also in Appendix A.

Finally, we will compute the last factor in (3) by means of the so called particle-particle Tamm-Dancoff Approximation (pp-TDA) formalism⁸, to be briefly described below.

The second matrix element entering Eq. (1) is written as

$${}_N\langle f | H_{e-r}^+ | int \rangle_{N+1} = \frac{e}{m_0} \sqrt{\frac{2\pi\hbar}{V\omega_f\eta_f^2}} \sum_{\alpha,\gamma} (\vec{\varepsilon}_f^* \cdot \vec{p}_{\alpha\gamma}^*) \left(\int e^{-i\vec{q}_f \cdot \vec{r}} \phi_{\alpha e}(\vec{r}) \phi_{\gamma h}(\vec{r}) d^3r \right) \times {}_N\langle f | h_\gamma e_\alpha | int \rangle_{N+1}. \quad (4)$$

Its computation involves similar band and orbital factors (see Appendix A). The last factor requires – besides the intermediate $(N + 1)$ -pair states, to be obtained from the pp-TDA equations – the knowledge of the N -pair excited states, which will be obtained from the ordinary or “particle-hole” RPA formalism⁸. The starting point for both RPA and pp-TDA schemes are the HF single-particle states.

A. The HF equations

We take for the HF single-particle functions the following ansatz:

$$\phi_\alpha^{e(h)} = \sqrt{\frac{2}{L}} \sin\left(\frac{\pi z}{L}\right) \sum_s C_{\alpha,s}^{e(h)} \chi_s(\vec{r}_\parallel), \quad (5)$$

where $0 \leq z \leq L$, $L = 12$ nm is the height of our disk-shaped qdot, \vec{r}_\parallel is the projection of \vec{r} onto the xy plane, and χ_s are the two-dimensional (2D) oscillator wave functions, given elsewhere¹². The $C_{\alpha,s}$ coefficients are obtained from the equations^{12,15}:

$$\sum_t \left\{ E_{es}^{(0)} \delta_{st} + \beta \sum_{\gamma \leq \mu_F^e} \sum_{u,v} [\langle s, u | 1/r | t, v \rangle - \langle s, u | 1/r | v, t \rangle] C_{\gamma,u}^e C_{\gamma,v}^e - \beta \sum_{\gamma \leq \mu_F^h} \sum_{u,v} \langle s, u | 1/r | t, v \rangle C_{\gamma,u}^h C_{\gamma,v}^h \right\} C_{\alpha,t}^e = E_{e\alpha} C_{\alpha,s}^e, \quad (6)$$

and a similar set of equations for the $C_{\alpha,s}^h$. Notice that the $E^{(0)}$ are 2D oscillator energies:

$$E_{es}^{(0)} = \hbar \sqrt{\omega_0^2 + \omega_c^2/4} \{2k_s + |l_s| + 1\} + \frac{\hbar \omega_c}{2} l_s + g_e \mu_B B S_z^e, \quad (7)$$

$$E_{hs}^{(0)} = \frac{m_e}{m_h} \hbar \sqrt{\omega_0^2 + \omega_c^2/4} \{2k_s + |l_s| + 1\} - \frac{m_e}{m_h} \frac{\hbar \omega_c}{2} l_s - g_h \mu_B B S_z^h, \quad (8)$$

where $\hbar \omega_0 = 3$ meV is the in-plane confinement, $\omega_c = eB/(m_e c)$ is the electron cyclotronic frequency, and g_e, g_h are Lande factors. We took parameters appropriate for GaAs: $m_e = 0.067m_0$, i. e. $\hbar \omega_c/B = 1.728$ meV/Teslas, the ratio of in-plane masses is $m_e/m_h = 0.067/0.11$, and $g_e \mu_B = -0.0173$ meV/Teslas, $g_h \mu_B = 0.0296$ meV/Teslas. In the g -factors, the effect of qdot height was approximately accounted for¹⁶.

On the other hand, the $\langle s, u | 1/r | t, v \rangle$ are Coulomb matrix elements taken over 2D oscillator wave functions¹², and the strength β is given by $0.8 e^2/(\kappa l_0)$, where:

$$l_0 = \sqrt{\frac{\hbar}{m_e \sqrt{\omega_0^2 + \omega_c^2/4}}}, \quad (9)$$

is the unit of length, $\kappa = 12.5$ is the dielectric constant, and the 0.8 coefficient takes care approximately of the effect on Coulomb interaction of averaging over the z coordinate¹⁷.

Equations (6) are solved iteratively. We start by occupying the lowest oscillator shells, construct the matrix inside brackets in (6), and iterate until convergence is reached. The occupation of HF levels is actualized after every 10 steps in accordance to the current values of the HF energies. 15 oscillator shells are used in the calculations, i. e. a total of 240 2D oscillator states.

B. The RPA equations

In the RPA⁸, we allow a general correlated ground state, $|RPA\rangle$, and the excited states are looked for in the form

$$\Psi = Q^\dagger |RPA\rangle, \quad (10)$$

where the Q^\dagger operator for CDE states is given by the expression

$$Q_{CDE}^\dagger = \sum_{\sigma,\lambda} (X_{\sigma\lambda}^e e_\sigma^\dagger e_\lambda + X_{\sigma\lambda}^h h_\sigma^\dagger h_\lambda - Y_{\lambda\sigma}^e e_\lambda^\dagger e_\sigma - Y_{\lambda\sigma}^h h_\lambda^\dagger h_\sigma). \quad (11)$$

The index λ runs over occupied HF states, and σ runs over unoccupied states. The X , Y coefficients are nonzero only for transitions respecting the selection rules, i.e. the spin projection doesn't change, and the change in angular momentum is fixed (a given multipolarity of the excitation). These coefficients satisfy the equations:

$$\begin{aligned} \sum_{\tau,\mu} \{ A_{\sigma\lambda,\tau\mu}^{ee} X_{\tau\mu}^e + A_{\sigma\lambda,\tau\mu}^{eh} X_{\tau\mu}^h + B_{\sigma\lambda,\mu\tau}^{ee} Y_{\mu\tau}^e + B_{\sigma\lambda,\mu\tau}^{eh} Y_{\mu\tau}^h \} &= \hbar\Omega X_{\sigma\lambda}^e, \\ \sum_{\tau,\mu} \{ A_{\sigma\lambda,\tau\mu}^{he} X_{\tau\mu}^e + A_{\sigma\lambda,\tau\mu}^{hh} X_{\tau\mu}^h + B_{\sigma\lambda,\mu\tau}^{he} Y_{\mu\tau}^e + B_{\sigma\lambda,\mu\tau}^{hh} Y_{\mu\tau}^h \} &= \hbar\Omega X_{\sigma\lambda}^h, \\ \sum_{\tau,\mu} \{ B_{\lambda\sigma,\tau\mu}^{ee} X_{\tau\mu}^e + B_{\lambda\sigma,\tau\mu}^{eh} X_{\tau\mu}^h + A_{\lambda\sigma,\mu\tau}^{ee} Y_{\mu\tau}^e + A_{\lambda\sigma,\mu\tau}^{eh} Y_{\mu\tau}^h \} &= -\hbar\Omega Y_{\lambda\sigma}^e, \\ \sum_{\tau,\mu} \{ B_{\lambda\sigma,\tau\mu}^{he} X_{\tau\mu}^e + B_{\lambda\sigma,\tau\mu}^{hh} X_{\tau\mu}^h + A_{\lambda\sigma,\mu\tau}^{he} Y_{\mu\tau}^e + A_{\lambda\sigma,\mu\tau}^{hh} Y_{\mu\tau}^h \} &= -\hbar\Omega Y_{\lambda\sigma}^h, \end{aligned} \quad (12)$$

in which $\hbar\Omega$ is the excitation energy, τ and μ are indexes similar to σ and λ , respectively, and the A and B matrices are given by^{12,15}:

$$\begin{aligned} A_{\sigma\lambda,\tau\mu}^{ee} &= (E_{e\sigma} - E_{e\lambda})\delta_{\sigma\tau}\delta_{\lambda\mu} + \beta(\langle\sigma, \mu|1/r|\lambda, \tau\rangle - \langle\sigma, \mu|1/r|\tau, \lambda\rangle), \\ A_{\sigma\lambda,\tau\mu}^{eh} &= -\beta\langle\sigma, \mu|1/r|\lambda, \tau\rangle, \\ B_{\sigma\lambda,\mu\tau}^{ee} &= \beta(\langle\sigma, \tau|1/r|\lambda, \mu\rangle - \langle\sigma, \tau|1/r|\mu, \lambda\rangle), \\ B_{\sigma\lambda,\mu\tau}^{eh} &= -\beta\langle\sigma, \tau|1/r|\lambda, \mu\rangle. \end{aligned} \quad (13)$$

Notice, for example, that in $A_{\sigma\lambda,\tau\mu}^{eh}$, σ and λ are electronic HF states, and τ, μ – hole states. A^{hh} has formally the same expression as A^{ee} , A^{he} the same as A^{eh} , etc. Let us stress also that Coulomb matrix elements over HF states enter the RPA equations (12), they can be computed from the matrix elements over oscillator states by means of the expansions (5). Usually, positive (physical) and negative (unphysical) excitation energies come from (12). The physical solutions annihilate the RPA ground state

$$Q|RPA\rangle = 0, \quad (14)$$

and satisfy the normalization condition

$$1 = \sum_{\sigma,\lambda} \{|X_{\sigma\lambda}^e|^2 + |X_{\sigma\lambda}^h|^2 - |Y_{\lambda\sigma}^e|^2 - |Y_{\lambda\sigma}^h|^2\}. \quad (15)$$

To evaluate the collective character of a state Ψ , we compute the matrix elements of the multipole operators: $\langle \Psi | D_l | RPA \rangle$. Collective states give significant transition strengths, whereas single-particle excitations give practically zero matrix elements. The multipole operator, D_l , is defined as:

$$D_l = e \sum_{\alpha, \gamma} \left\{ d_{\alpha\gamma}^{hl} h_{\alpha}^{\dagger} h_{\gamma} - d_{\alpha\gamma}^{el} e_{\alpha}^{\dagger} e_{\gamma} \right\}, \quad (16)$$

where

$$\begin{aligned} d_{\alpha\gamma}^l &= \langle \alpha | \rho^{l|} e^{il\theta} | \gamma \rangle; \quad l \neq 0, \\ &= \langle \alpha | \rho^2 | \gamma \rangle; \quad l = 0. \end{aligned} \quad (17)$$

ρ and θ are polar coordinates in the xy plane. Detailed expressions for $d_{\alpha\gamma}^l$ are given in Appendix B.

Multipole matrix elements are computed from the RPA amplitudes in the following way:

$$\langle \Psi | D_l | RPA \rangle = e \sum_{\sigma, \lambda} \left\{ X_{\sigma\lambda}^{h*} d_{\sigma\lambda}^{hl} - X_{\sigma\lambda}^{e*} d_{\sigma\lambda}^{el} + Y_{\lambda\sigma}^{h*} d_{\lambda\sigma}^{hl} - Y_{\lambda\sigma}^{e*} d_{\lambda\sigma}^{el} \right\}. \quad (18)$$

They fulfill the energy-weighted sum rules⁸

$$\begin{aligned} \sum_{\Psi} \hbar \Omega_{\Psi} \left\{ |\langle \Psi | D_l | RPA \rangle|^2 + |\langle \Psi | D_{-l} | RPA \rangle|^2 \right\} &= 2\hbar^2 e^2 l^2 \left\{ \frac{1}{m_e} \sum_{\lambda \leq \mu_F^e} \langle \lambda | (r^2)^{|l|-1} | \lambda \rangle \right. \\ &\quad \left. + \frac{1}{m_h} \sum_{\lambda \leq \mu_F^h} \langle \lambda | (r^2)^{|l|-1} | \lambda \rangle \right\}, \end{aligned} \quad (19)$$

for $l \neq 0$, and

$$\sum_{\Psi} \hbar \Omega_{\Psi} |\langle \Psi | D_0 | RPA \rangle|^2 = 2\hbar^2 e^2 \left\{ \sum_{\lambda \leq \mu_F^e} \langle \lambda | \frac{r^2}{m_e} | \lambda \rangle + \sum_{\lambda \leq \mu_F^h} \langle \lambda | \frac{r^2}{m_h} | \lambda \rangle \right\}, \quad (20)$$

for $l = 0$. The μ_F 's are Fermi levels. Thus, $\lambda \leq \mu_F$ means that the sum runs over occupied HF states. Explicit evaluation of the r. h. s. of (19,20) is done in Appendix B.

Spin excitations can also be built on within the RPA formalism. For example, a state with $\Delta S_{ez} = 1$, $\Delta S_{hz} = 0$ can be obtained from a Q^{\dagger} like (11) with only electron operators, such that the transitions satisfy the spin selection rule. It should be noticed, however, that the simple combination of one-particle excitations in Eq. (11) does not allow us to construct “ $2p - 2h$ ” excited states with $\Delta S_{ez} = 1$, $\Delta S_{hz} = -1$, for example, entering the final states of Raman SDE processes.

C. pp-TDA

The pp-TDA scheme allows us to build up states with $2N + 2$ particles starting from the the ground state of the N -pair system⁸. Notice that there are 12 possibilities for the

added pair of particles. We can add, for example, an e-e pair with various spin orientations. In this subsection, we focus on the situations where an optically created e-h pair is added. That is, only the following two possibilities are considered: $e\uparrow h\downarrow$ or $e\downarrow h\uparrow$.

The Q^\dagger operator, analogous to Eq. (11), is written in the following form:

$$Q^\dagger = \sum_{\sigma, \tau} V_{\sigma\tau}^{(N+1)} e_\sigma^\dagger h_\tau^\dagger, \quad (21)$$

where, as before, σ and τ label states above the Fermi levels. Q^\dagger acts on the RPA ground state to produce states with $N + 1$ pairs. The V coefficients satisfy the equations:

$$(\hbar\Omega - E_\sigma^e - E_\tau^h) V_{\sigma\tau}^{(N+1)} = -\beta \sum_{\sigma', \tau'} \langle \sigma, \tau | 1/r | \sigma', \tau' \rangle V_{\sigma'\tau'}^{(N+1)}. \quad (22)$$

The quantity $\hbar\Omega$ gives the excitation energy, measured with respect to the $|RPA\rangle$ N -pair state: $E(N + 1) - E_{RPA}(N)$.

RPA and pp-TDA excitations energies and coefficients X , and V are to be used in the computation of Raman amplitudes.

D. Raman scattering in CDE channels

The inelastic scattering of light, schematically represented in Fig. 1 (a), is characterized by a Raman shift: $\hbar\omega_i - \hbar\omega_f = E_f - E_i = \hbar\Omega_f$. The amplitude for the process is given by Eq. (1). This amplitude will depend on the scattering angles.

To state a convention, the dot plane will define the xy plane, and the magnetic field – the positive z -axis. The incident light comes from the $z < 0$ subspace, forming an angle ϕ_i with the z axis. The \vec{q}_i , \vec{B} pair of vectors define the xz plane, i. e. the projection $\vec{q}_{i\parallel}$ is oriented along the positive x axis. The emitted light goes back to the $z < 0$ subspace. It is characterized by angles ϕ_f with the z -axis, and θ_f in the xy plane. We will take, for the incident light:

$$\begin{aligned} q_{i\parallel} &= q_i \sin \phi_i, \\ \varepsilon_{iy} &= 1, \end{aligned} \quad (23)$$

whereas for the scattered light: $q_{f\parallel} = q_f \sin \phi_f$. We will distinguish two situations: (i) The “parallel” light polarization, in which:

$$\begin{aligned} \varepsilon_{fx} &= -\sin \theta_f, \\ \varepsilon_{fy} &= \cos \theta_f, \end{aligned} \quad (24)$$

and (ii) The “perpendicular” light polarization, where:

$$\begin{aligned} \varepsilon_{fx} &= \cos \phi_f \cos \theta_f, \\ \varepsilon_{fy} &= \cos \phi_f \sin \theta_f. \end{aligned} \quad (25)$$

Below, we give an explicit expression for the matrix element of the H_{e-r}^- hamiltonian:

$${}_{N+1}\langle int|H_{e-r}^-|i\rangle_N = \frac{e}{m_0}\sqrt{\frac{2\pi\hbar}{V\omega_i\eta_i^2}}\sum_{\sigma,\tau}band_{\sigma,\tau}^{(i)}\times orbital_{\sigma,\tau}^{(i)}\times V_{\sigma,\tau}^{(N+1)*}. \quad (26)$$

The band and orbital factors are evaluated in Appendix A. The energy denominator in the scattering amplitude will be written in the form:

$$\hbar\omega_i - (E_{int} - E_i) = \hbar\omega_i - E_{gap} - \hbar\Omega_{int}^{(N+1)}, \quad (27)$$

where $\hbar\Omega_{int}$ is the eigenvalue coming from the pp-TDA equations, and $E_{gap} = 1560$ meV is a nominal band gap.

The matrix element of the H_{e-r}^+ operator, has a bit more cumbersome expression:

$$\begin{aligned} {}_N\langle f|H_{e-r}^+|int\rangle_{N+1} = & -\frac{e}{m_0}\sqrt{\frac{2\pi\hbar}{V\omega_f\eta_f^2}}\sum_{\sigma,\tau}\sum_{\sigma',\lambda}\delta(\sigma,\sigma')band_{\lambda\tau}^{(f)}\times orbital_{\lambda\tau}^{(f)}\times V_{\sigma\tau}^{(N+1)}X_{\sigma'\lambda}^{e*} \\ & -\frac{e}{m_0}\sqrt{\frac{2\pi\hbar}{V\omega_f\eta_f^2}}\sum_{\sigma,\tau}\sum_{\tau',\lambda}\delta(\tau,\tau')band_{\sigma\lambda}^{(f)}\times orbital_{\sigma\lambda}^{(f)}\times V_{\sigma\tau}^{(N+1)}X_{\tau'\lambda}^{h*}. \end{aligned} \quad (28)$$

The interpretation is, however, straightforward. Let us take the first term. The first sum runs over e-h states (σ, τ) , both above the Fermi levels, entering the pp-TDA function $|int\rangle_{N+1}$. $V_{\sigma\tau}^{(N+1)}$ are the corresponding coefficients. The second sum represents the electronic excitation part of the RPA function $|f\rangle_N$. λ is an electronic state below μ_F^e , and σ' an state above μ_F^e . The transition from $|int\rangle_{N+1}$ to $|f\rangle_N$ is caused by a pair of annihilation operators he . It is evident that the subindexes should be $h_\tau e_\lambda$, and thus $\sigma' = \sigma$.

Amplitudes for backscattering processes, in which $\phi_f = \phi_i$, and $\theta_f = \pi$, will be computed.

III. RESULTS

A. Properties of the HF ground state

We give in this sub-section a few qualitative results that follow from the HF calculations.

We show in Fig. 2 a subset of the HF single-particle levels at $B = 1$ T. Fermi energies are represented as dotted lines. Apart from an overall downward shift, we observe only a slight deformation of free oscillator shells due to Coulomb interactions. The Zeeman splitting is not resolved in the figure scale, thus spin-up and -down levels are simultaneously occupied. As a result, total electron and hole spins remain equal to zero when the magnetic field is varied between zero and 2 T. In fact, very low spin polarizations persist up to higher magnetic fields, of the order of 20 T.¹⁴ The total ground-state angular momentum is also zero in this magnetic field range, and persists up to very high B , as a prelude to the formation of e-h pairs in zero relative angular momentum states, which maximize Coulomb attraction.

Let us stress also that Fig. 2 qualitatively predicts that single-particle excitations (SPE) with $\Delta L_z = \pm 2$ (“quadrupole”-like, represented by arrows in the figure) are lower in energy than “monopole” ($\Delta L_z = 0$) or “dipole” ($\Delta L_z = \pm 1$) excitations at $B = 1$ T. This fact is corroborated by the RPA calculations, see below. The energetic cost of adding an e-h pair with $l_e + l_h = 0$ is, according to Fig. 2, around 15 meV (plus E_{gap}). A value confirmed by the TDA results.

Electron and hole densities at $B = 0$ and 2 T are drawn in Fig. 3. The small differences between both densities are due to the differences between electron and hole in-plane masses. The maximum value, around 7×10^{11} pairs/cm², is typical of excitonic systems. Notice also that density oscillations, related to shell-filling effects, are smoothed as B is increased. This fact is due to the increasing occupations of states in the first Landau level, which wave functions have no radial nodes.

B. Multipole excitations and renormalization of the absorption edge

CDE of various multiplicities in the N -pair system are obtained from the RPA computations. We show in Fig. 4 the monopole sector, which is the most relevant for Raman CDE processes. States with more than 5 % contribution to the energy-weighted sum rule (19) are represented in the figure as triangles. They will be called “collective” excitations. They form three well defined bands accounting for, approximately, 7, 35 and 5% of the sum rule. The rest of the monopole strength is divided among 200 states with excitation energy lower than 30 meV. Fig. 4 shows also the lowest monopole SPE (triangles plus dotted line). A complex pattern of probability transfer between colliding levels, as the magnetic field is varied, is reflected in Fig. 4 in the form of abrupt variations of the number of collective levels. The situation is similar to the behavior of the dipole strength in the biexciton¹⁸.

Dipole and quadrupole collective levels and the corresponding SPE in these sectors are shown in Fig. 5. One sees that dipole excitations are, as a rule, lower than monopole and quadrupole collective CDE, but the quadrupole SPE are lower at $B = 1$ T, as mentioned above with regard to Fig. 2.

We show in Fig. 6 a few results following from the pp-TDA calculations. In the upper figure, the lowest $\hbar\Omega_{int}$ for the intermediate state with $N + 1$ pairs, in which the added pair has $l_e + l_h = 0$, is drawn. This magnitude can be taken as the renormalization of the absorption edge due to the background of N electron-hole pairs. Let us stress that there are two main effects contributing to this magnitude. The first is the blue shift induced by Fermi statistics, i. e. the added pair should occupy higher HF single-particle states. The second is the red shift caused by Coulomb (attractive) interactions. As can be seen in this figure, for $N = 42$ the net result is a blue shift of 12 - 16 meV. The apparent kinks are signals of ground-state rearrangements as the magnetic field is varied.

The lowest part of Fig. 6 shows the dependence on N of the edge renormalization at $B = 1$ T. It grows from 3 meV for 12 pairs up to 14 meV for the 42-pair system. That is, at a rate of 0.3 meV per pair in the dot. This magnitude can be used as a complementary way of determining the mean number of pairs in the dot.

C. Raman spectra in CDE channels

Let us consider Raman processes in which the final states are CDE. The first important question we would like to address is the role played by collective and SPE in resonant Raman amplitudes.

We show in Fig. 7 the Raman differential cross section, computed from

$$\frac{d^2\sigma}{d\Lambda_f d\omega_f} = \frac{V^2 \omega_f^3 \eta_f \eta_i^3}{4\pi^2 c^4 \omega_i \hbar N_i} \sum_f |A_{fi}|^2 \delta(E_i + \hbar\omega_i - E_f - \hbar\omega_f), \quad (29)$$

in which $d\Lambda_f$ is the solid angle element in the direction of the dispersed light. We will use a smearing of the delta function as follows:

$$\delta(x) = \frac{\Gamma_f/\pi}{x^2 + \Gamma_f^2}, \quad (30)$$

with a phenomenological $\Gamma_f = 0.5$ meV.

The spectra in Fig. 7 are computed under conditions of normal incidence ($\phi_i = \phi_f = 0$, only monopole final states are excited) and parallel light polarization. The latter is supposed to disentangle collective CDE modes from SDE in electronic qdots under non-resonant scattering¹⁹. The monopole strengths are also included in the figure for comparison.

The upper figure shows results at $B = 1$ T. There are always Raman peaks associated to the more collective CDE states, although their magnitude rapidly vary with the incident laser frequency. The overall behavior, which is apparent in this figure, is that low-energy weakly collective or SPE are favored at “extreme resonance”, i. e. when $\hbar\omega_i$ is near 1574 meV in this situation, whereas 30 meV above the effective band gap high-energy collective or weakly collective CDE give the strongest peaks.

Notice that the maximum peak intensities under extreme resonance are reached for laser frequencies a few meV above the renormalized band gap. Thus, as the laser frequency moves above 1574 meV, the amplitudes corresponding to weakly collective or SPE initially increase, but further experience a sudden drop.

In the lower part of Fig. 7, the spectra at $B = 2$ T are drawn. We notice variations in the peak distributions as compared to the $B = 1$ T results. Notice also that, in both spectra, the strongest CDE state is not seen as a distinct peak for $\hbar\omega_i = 1600$ meV.

The qualitative conclusions to be extracted from Fig. 7 are thus the following: (a) Comparable Raman intensities for strongly collective and for weakly collective states (even for SPE at intermediate excitation energies), (b) A complex pattern of variations of the Raman intensities as the frequency of the incident laser or the magnetic field is varied. Distinct peaks are seen only in certain intervals of these magnitudes, and (c) A richer structure of the Raman spectra as compared with the charged quantum dots.

The second important point to discuss, from the qualitative point of view, is the excitation of high multipolarity modes at non-zero momentum transfer. We notice that the light wave vector is around $8 \times 10^3 \text{ nm}^{-1}$ in the present situation. The maximum momentum transfer is thus $1.6 \times 10^4 \text{ nm}^{-1}$ in backscattering geometry. We show in Fig. 8 the quadrupole spectra at $B = 1$ T in the parallel light polarization configuration and momentum transfer equal to $8 \times 10^3 \text{ nm}^{-1}$ ($\phi_i = \phi_f = \pi/6$). Of course, in an experimental curve all the multipolarities come together. We separate the quadrupole spectra to simplify the analysis.

First, we notice that quadrupole Raman intensities are 1/10 of monopole ones. On qualitative grounds, one expects quadrupole intensities of order $N_{states}^2 (q_{i\parallel} D)^4$, where $D \approx 90$ nm is the system diameter, and N_{states} is the number of intermediate states participating in the process. $(q_{i\parallel} D)^4$ provides a factor 10^{-2} , but the number of states contributing to quadrupole processes is roughly three times the states contributing to monopole processes (intermediate states with excess angular momentum 0, +1, and +2 in the $\Delta l = +2$ case,

for example). Thus $N_{states}^2(q_{i\parallel}D)^4 \approx 10^{-1}$. Second, we observe an asymmetry between the $\Delta l = -2$ and $\Delta l = 2$ spectra. Most of the $\Delta l = -2$ peaks correspond to SPE or weakly collective states. The $\Delta l = 2$ peaks, two or three times more intense, are concentrated around collective states, which strengths are more uniformly distributed. The most collective CDE state with $\Delta l = 2$ shows up as a distinct peak only in a thin range of frequencies. Other multipoles show similar behavior.

Thus, the conclusions coming from Fig. 8 are the following: (a) The intensity of CDE Raman peaks with multipolarity l are proportional to $(|l| + 1)^2(q_{i\parallel}D)^{2|l|}$, and (b) Negative- l peaks correspond mainly to very weakly collective or SPE states. The peak associated to the most collective CDE state is well defined practically at any $\hbar\omega_i$. On the other hand, positive- l peaks are stronger and show a dominance of collective states.

A third interesting question to be addressed is related to the modes excited when the dispersed light polarization is orthogonal to the polarization of the incident light. The results for monopole states at $B = 1$ T are presented in Fig. 9. Under extreme resonance, we observe peaks associated to SPE modes with excitation energies lower than 12 meV. In particular, the lowest SPE at 4 meV is clearly distinguished. Raman signals due to CDE states are strongly suppressed in these conditions. 30 meV above extreme resonance, the dominant peaks are located at higher excitation energies. They correspond to SPE or weakly collective states.

IV. CONCLUSIONS

We have computed the Raman amplitudes for the light scattered of a qdot which contains 42 e-h pairs. In an attempt to identify the states giving rise to the strongest peaks, we compared the Raman intensities with the multipole strengths. The result is that both collective and SPE states play important roles in Raman spectra. Their relative weight in the spectra is seen to strongly depend on the external magnetic field, the polarization of the scattered light and the frequency of the incident light. Taken in a wider context, this conclusion suggests caution when making an assignment to an experimental Raman peak, and urges for theoretical calculations in parallel to the experiments.

The explicit construction of the wave functions for the intermediate states, always in the framework of mean-field time-dependent approximations, allows us to consider extreme as well as non extreme resonance conditions. In the same way, the formalism allows for any wave momentum transfer or any kind of light polarization.

We can not presently consider SDE final states. The reason has been explained briefly in the text: the SDEs are “2p-2h” states, which can not be modeled by the RPA approximation adopted in this work. It shall be said, however, that none of the papers 3 or 4 accounted for valence-band mixing effects in the intermediate hole state in Raman SDE channels.

However, on qualitative grounds, it can be argued that SDE final states shall give strong Raman peaks, may be even stronger than CDE states. The argument goes as follows. It may be seen that the factor determining the Raman amplitude is in fact the orbital factor, i. e. the overlapping between the electron and hole wave functions. In the symmetric, $N_e = N_h$, system we are studying, the overlapping is high in the intermediate states (both e and h above the Fermi levels), but low for CDE final states because one of the annihilated particles is above its Fermi level, and the other is below. For SDE states, however, both the

annihilated e and h are below their Fermi levels, and the overlapping may be high. Thus, Raman SDE amplitudes could be even stronger than CDE amplitudes.

In the electronic qdots, Raman scattering in SDE channels goes through hole band mixing. Apart from the low overlapping in final states, one would expect the amplitude to be proportional to the light hole component of the hole wave function. Due to the fact that the Coulomb interaction is diagonal in the band indexes, a strong electronic background could depress valence band mixing, thus making SDE amplitudes even weaker. Research along this direction is in progress.

ACKNOWLEDGMENTS

Part of this work was carried out at the Abdus Salam ICTP. A. D. and A. G. acknowledge the ICTP Associate and Federation Schemes Office for support.

APPENDIX A: EVALUATION OF BAND AND ORBITAL FACTORS

We give in this Appendix the expressions for the band and orbital factors entering Eqs. (3) and (4). The ratio of the band factor $\vec{\varepsilon}_i \cdot \vec{p}_{\alpha\gamma}$ to the magnitude iP , where P is the interband GaAs constant, is given in Tab. I. $S_z = \pm 1/2$ is the spin projection over the z axis.

Conventionally, we assign $S_z^h = -1/2$ to the $m_j = 3/2$ electron state in the valence band. The ε_{\pm} components are defined as

$$\varepsilon_{\pm} = \mp \frac{\varepsilon_x \mp i\varepsilon_y}{\sqrt{2}}. \quad (\text{A1})$$

The band factor entering Eq. (4), i. e. $\vec{\varepsilon}_f^* \cdot \vec{p}_{\alpha\gamma}^*$, can be also obtained from Table I if we replace ε_+ by ε_- and viceversa.

On the other hand, the orbital factor in Eq. (3) is computed from the HF one-particle functions, Eq. (5). Substituting (5) into the expression for the band factor, Eq. (3), and making use of the expansion:

$$e^{i\vec{q}_i \cdot \vec{r}} \approx 1 + i\vec{q}_i \cdot \vec{r}_{\parallel} - \frac{1}{2}(\vec{q}_i \cdot \vec{r}_{\parallel})^2, \quad (\text{A2})$$

where \vec{r}_{\parallel} means the projection of \vec{r} onto the xy plane, we get

$$\begin{aligned} \int e^{i\vec{q}_i \cdot \vec{r}} \phi_{\alpha e}^*(\vec{r}) \phi_{\gamma h}^*(\vec{r}) d^3r &\approx \sum_{s,t} C_{\alpha s}^{e*} C_{\gamma t}^{h*} \left\{ \langle k_s, l_s | 1 - \frac{q_{i\parallel}^2}{4} d_0 | k_t, -l_t \rangle + \right. \\ & i \frac{q_{i\parallel}}{2} \langle k_s, l_s | e^{-i\theta_i} d_1 + e^{i\theta_i} d_{-1} | k_t, -l_t \rangle \\ & \left. - \frac{(q_{i\parallel})^2}{8} \langle k_s, l_s | e^{-2i\theta_i} d_2 + e^{2i\theta_i} d_{-2} | k_t, -l_t \rangle \right\}. \end{aligned} \quad (\text{A3})$$

In this last equation, d_l are the one-particle multipole operators, which explicit expression is given in Appendix B. The k_s and l_s are, respectively, the radial and orbital quantum

numbers of the 2D oscillator state χ_s . The angle θ_i is by definition equal to zero, i. e. the z axis is oriented along $\vec{q}_{i\parallel}$.

The orbital factor entering Eq. (4) can be obtained formally from (A3) upon substituting i by f and taking the complex conjugate of the whole expression.

APPENDIX B: MULTIPOLE MATRIX ELEMENTS AND SUM RULES

The evaluation of one-particle elements, $d_{\alpha,\gamma}^l$, requires the expansion (5) for HF functions:

$$d_{\alpha,\gamma}^l = \sum_{s,t} C_{\alpha s}^* C_{\gamma t} d_{st}^l, \quad (\text{B1})$$

where the elements d_{st}^l , taken over oscillator functions, are given, when $l = 0$, by:

$$\begin{aligned} \langle k_s, l_s | \frac{d_0}{l_0^2} | k_t, l_t \rangle &= \delta(l_s, l_t) \left\{ (2k_t + |l_t| + 1) \delta(k_s, k_t) - \sqrt{(k_t + 1)(k_t + |l_t| + 1)} \delta(k_s, k_t + 1) \right. \\ &\quad \left. - \sqrt{k_t(k_t + |l_t|)} \delta(k_s, k_t - 1) \right\}. \end{aligned} \quad (\text{B2})$$

Whereas, for $l > 0$:

$$\begin{aligned} \langle k_s, l_s | \frac{d_l}{l_0^l} | k_t, l_t \rangle &= \delta(l_s, l_t + l) \sum_{r=0}^{\text{Min}(l, k_t)} (-1)^r \frac{l!}{(l-r)!r!} \sqrt{\frac{k_t!}{(k_t + |l_t|)!} \frac{(k_t - r + |l_t + l|)!}{(k_t - r)!}} \\ &\quad \times \delta(k_s, k_t - r); \quad l_t \geq 0, \\ &= \delta(l_s, l_t + l) \sum_{r=0}^{\text{Min}(l, k_s)} (-1)^r \frac{l!}{(l-r)!r!} \sqrt{\frac{k_s!}{(k_s + |l_t + l|)!} \frac{(k_s - r + |l_t|)!}{(k_s - r)!}} \\ &\quad \times \delta(k_t, k_s - r); \quad l_t \leq -l, \\ &= \delta(l_s, l_t + l) (-1)^{k_s - k_t} \sum_{r=0}^{\text{Min}(l - |l_t|, k_t)} \frac{(l - |l_t|)!}{(l - |l_t| - r)!r!} \frac{|l_t|!}{(|l_t| - k_s + k_t - r)!} \\ &\quad \times \sqrt{\frac{k_t!}{(k_t + |l_t|)!} \frac{k_s!}{(k_s + |l_t + l|)!} \frac{(k_t - r + l)^2}{(k_t - r)!^2}} \Theta(k_s - k_t + r); \\ &\quad -l < l_t < 0. \end{aligned} \quad (\text{B3})$$

Where $\Theta(x) = 1$ for $0 \leq x \leq \text{Min}(|l_t|, k_s)$ and zero otherwise. Finally, for $l < 0$, we get:

$$\langle k_s, l_s | d_l | k_t, l_t \rangle = \langle k_t, l_t | d_{|l|} | k_s, l_s \rangle^*. \quad (\text{B4})$$

On the other hand, the elements $\langle \lambda | (r^2)^\xi | \lambda \rangle$, entering the r. h. s. of the sum-rule equations (19-20) are evaluated as:

$$\langle \lambda | (r^2)^\xi | \lambda \rangle = \sum_{s,t} C_{\lambda s}^* C_{\lambda t} \langle s | (r^2)^\xi | t \rangle, \quad (\text{B5})$$

where:

$$\begin{aligned} \langle k_s, l_s | \left(\frac{r^2}{l_0^2} \right)^\xi | k_t, l_t \rangle &= \delta(l_s, l_t) \sqrt{\frac{k_s! k_t!}{(k_s + |l_s|)! (k_t + |l_s|)!}} \sum_{m=0}^{\text{Min}(\xi, k_s)} \sum_{n=0}^{\text{Min}(\xi, k_t)} (-1)^{m+n} \\ &\quad \times \delta(k_s - m, k_t - n) \frac{\xi!^2}{(\xi - m)! m! (\xi - n)! n!} \frac{(k_t - n + |l_s| + \xi)!}{(k_t - n)!}. \end{aligned} \quad (\text{B6})$$

REFERENCES

- ^a Electronic address: gran@ceaden.edu.cu
- ^b Electronic address: agonzale@cidet.icmf.inf.cu
- ^c Electronic address: eariel@raman.ff.oc.uh.cu
- ¹ D. J. Lockwood, P. Hawrylak, P. D. Wang et. al., Phys. Rev. Lett. **77**, 354 (1996).
- ² C. Schuller, K. Keller, G. Biese et. al., Phys. Rev. Lett. **80**, 2673 (1998).
- ³ C. Steinebach, C. Schuller, and D. Heitmann, Phys. Rev. **B 59**, 10240 (1999).
- ⁴ M. Barranco, L. Colleti, E. Lipparini et. al., Phys. Rev. **B 61**, 8289 (2000).
- ⁵ A. Delgado and A. Gonzalez, to be submitted.
- ⁶ J. C. Kim and J. P. Wolfe, Phys. Rev. B **57**, 9861 (1998).
- ⁷ A. Wojs, P. Hawrylak, S. Fafard, and L. Jacak, Phys. Rev. **B 54**, 5604 (1996).
- ⁸ P. Ring and P. Schuck, The nuclear many-body problem, Springer-Verlag, New-York (1980).
- ⁹ E. Menéndez-Proupin, C. Trallero-Giner and S. E. Ulloa, Phys. Rev. **B 60**, 16747 (1999).
- ¹⁰ E. Menéndez-Proupin, Inelastic light scattering in semiconductor quantum dots, Ph. D. Thesis, Havana University (2000).
- ¹¹ H. D. M. Davies, J. C. Harris, J. F. Ryan, and A. J. Turberfield, Phys. Rev. Lett. **78**, 4095 (1997).
- ¹² A. Delgado, L. Lavin, R. Capote and A. Gonzalez, Physica E **8**, 342 (2000).
- ¹³ H. A. Nickel, T. Yeo, C. J. Meining et. al., cond-mat/0106277.
- ¹⁴ B. A. Rodriguez and A. Gonzalez, Phys. Rev. B **63** 205324 (2001).
- ¹⁵ A. Delgado, Giant dipole resonances in quantum dots, M. Sc. Thesis, Inst. for Nuclear Sci. and Tech., Havana (2000).
- ¹⁶ We use a parametrization by B. Rodriguez of the experimental g values for quantum wells given in S. P. Najda, S. Takeyama, N. Miura et. al., Phys. Rev. B **40**, 6189 (1989); M.J. Snelling, G. P. Flinn, A.S. Plaut, R. T. Harley, A. C. Tropper, R. Eccleston, and C. C. Phillips, Phys. Rev. B **44**, 11345 (1991); M. J. Snelling, E. Blackwood, C. J. McDonagh, R. T. Harley, and C. T. B. Foxon, Phys. Rev. B **45**, 3922 (1992); N. J. Traynor, R. J. Warburton, M. J. Snelling, and R. T. Harley, Phys. Rev. B **55**, 15701 (1997); M. Seck, M. Potemski, and P. Wyder, Phys. Rev. B **56**, 7422 (1997).
- ¹⁷ A. H. MacDonald and G. C. Aers, Phys. Rev. **B 29**, 5976 (1984).
- ¹⁸ R. Perez and A. Gonzalez, J. Phys.: Condens. Matter **13**, L539 (2001).
- ¹⁹ S. Katayama and T. Ando, J. Phys. Soc. Jpn. **54**, 1615 (1985).

TABLES

$S_{z\alpha}^e \setminus S_{z\gamma}^h$	-1/2	1/2
1/2	ε_{+i}	0
-1/2	0	ε_{-i}

TABLE I. The quotient $\vec{\varepsilon}_i \cdot \vec{p}_{\alpha\gamma}/(iP)$.

FIGURES

FIG. 1. (a) Inelastic light scattering leading to final states which are CDE of the ground state. (b) An example of Raman scattering in SDE channels.

FIG. 2. A set of electron and hole HF levels at $B = 1$ T. The Fermi energies are indicated as dotted lines. The less energetic transitions with $\Delta L_z = \pm 2$ are represented by arrows.

FIG. 3. Electron and hole densities in the HF ground state.

FIG. 4. Monopole collective CDEs of the N -pair system and the lowest SPE.

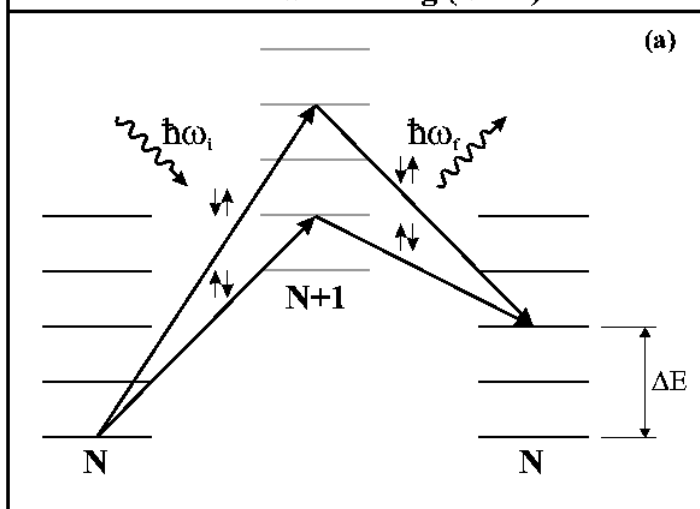
FIG. 5. Dipole and quadrupole collective CDEs and the lowest SPEs.

FIG. 6. Absorption edge renormalization: (a) As a function of B for $N = 42$, and (b) As a function of N for $B = 1$ T.

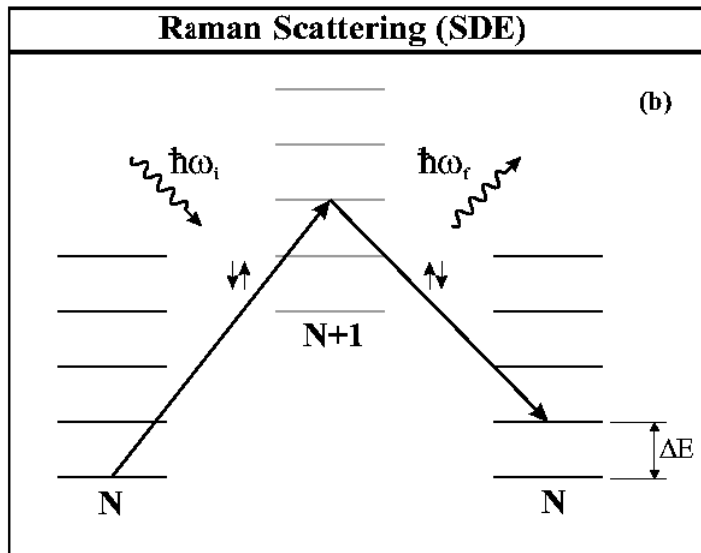
FIG. 7. Raman spectra under conditions of normal incidence and parallel polarization. Only final CDE states are considered.

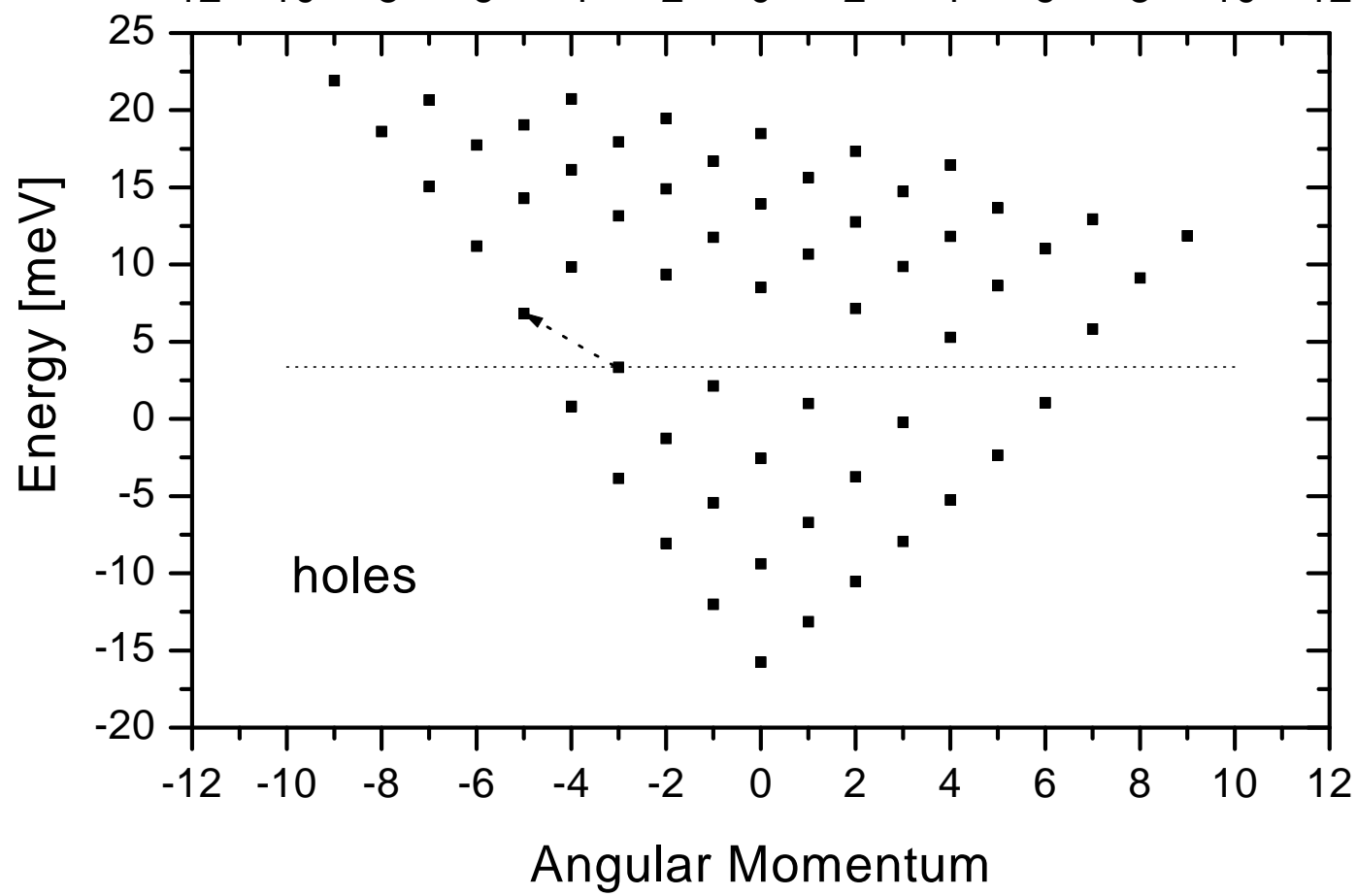
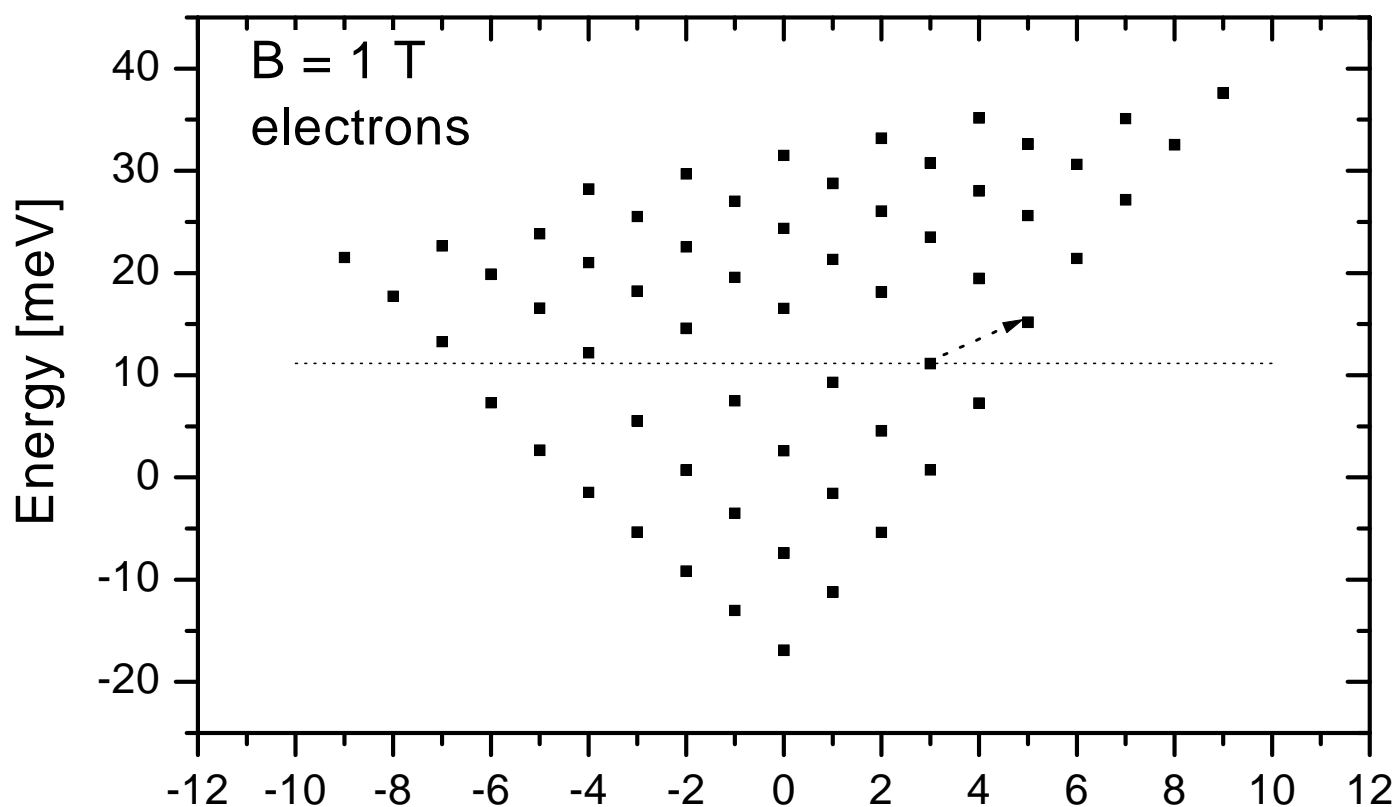
FIG. 8. Raman spectra of quadrupole CDE states. $\phi_i = \phi_f = \pi/6$ and parallel light polarization geometry.

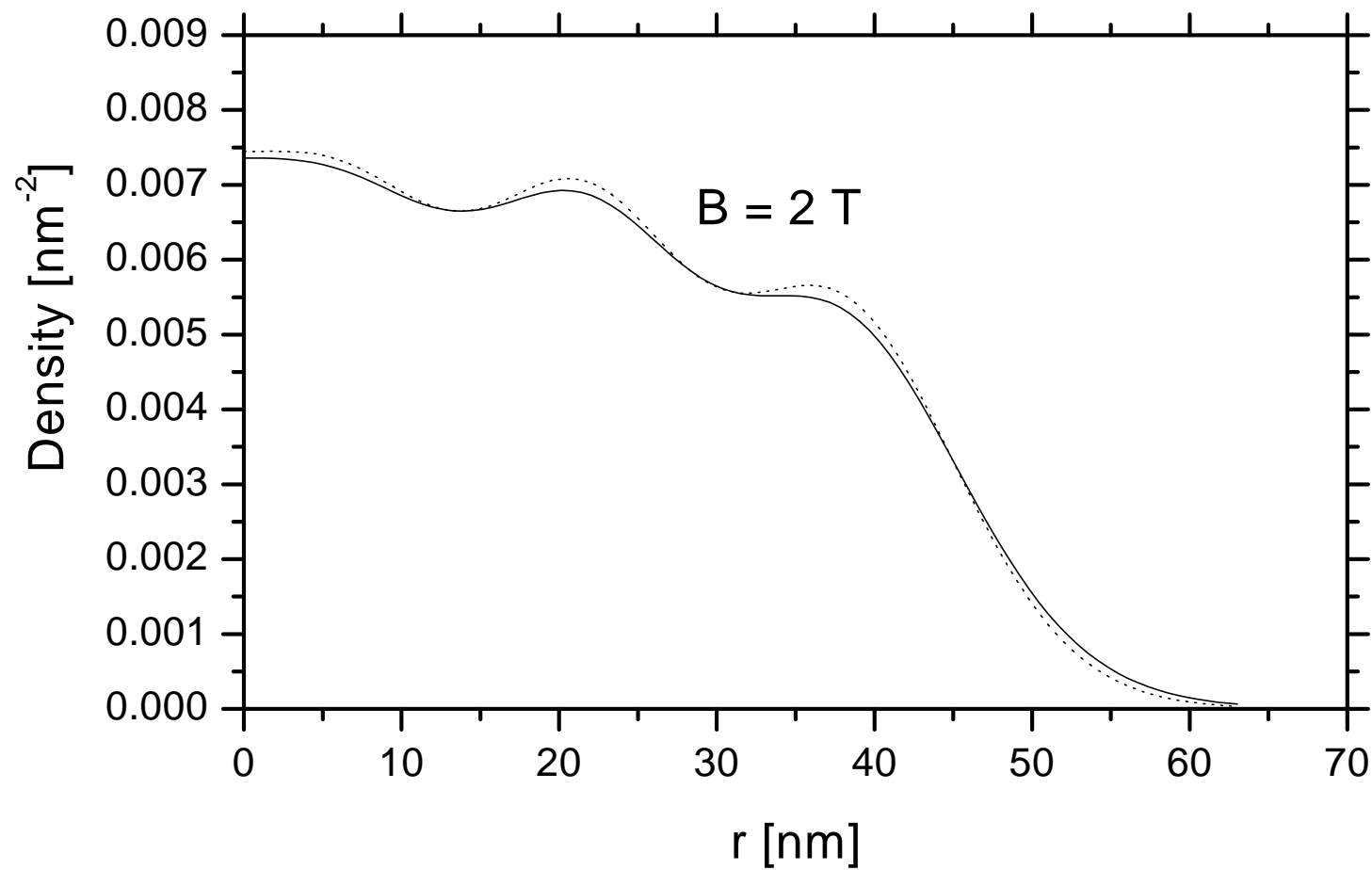
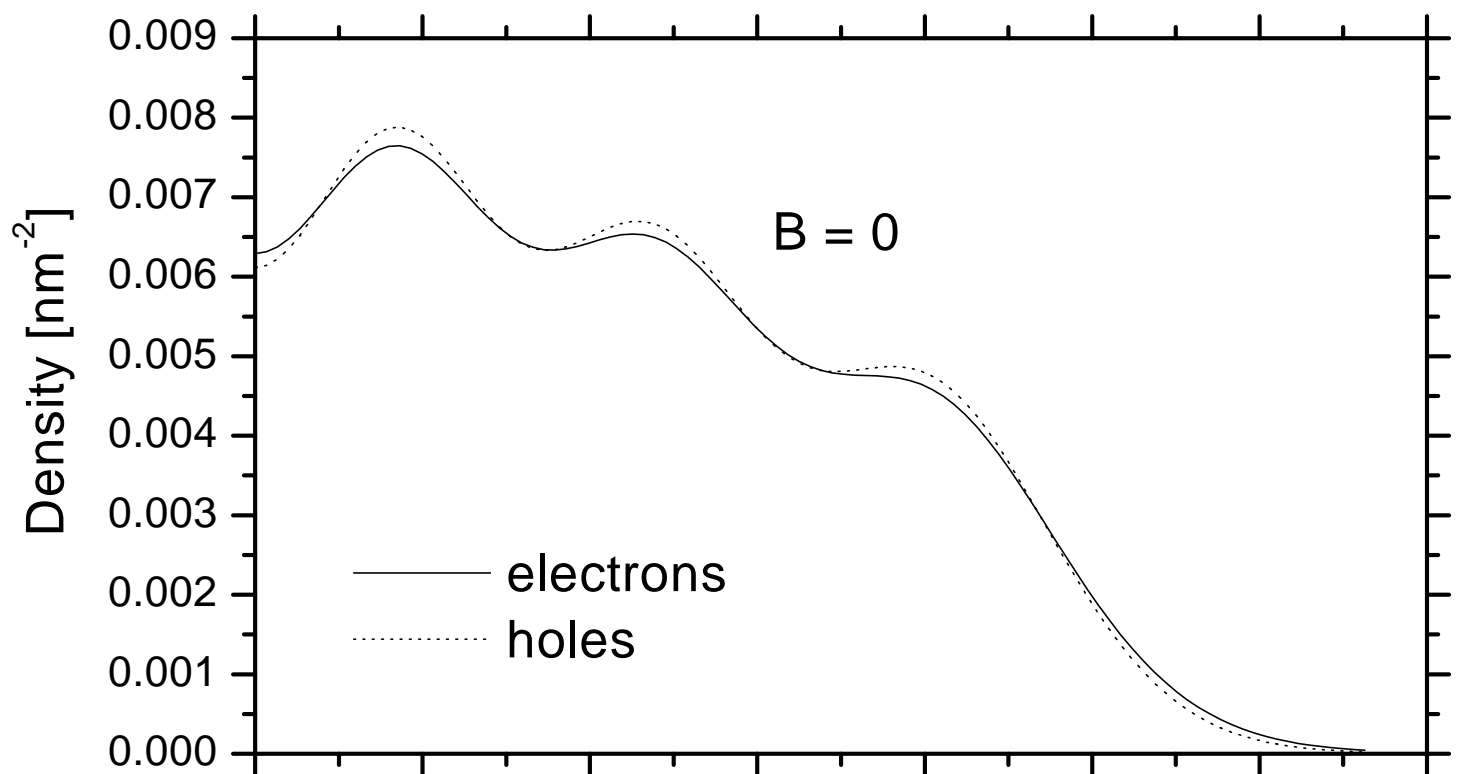
FIG. 9. The same as in Fig. 7, but the polarization of the scattered light is orthogonal to the polarization of the incident light.

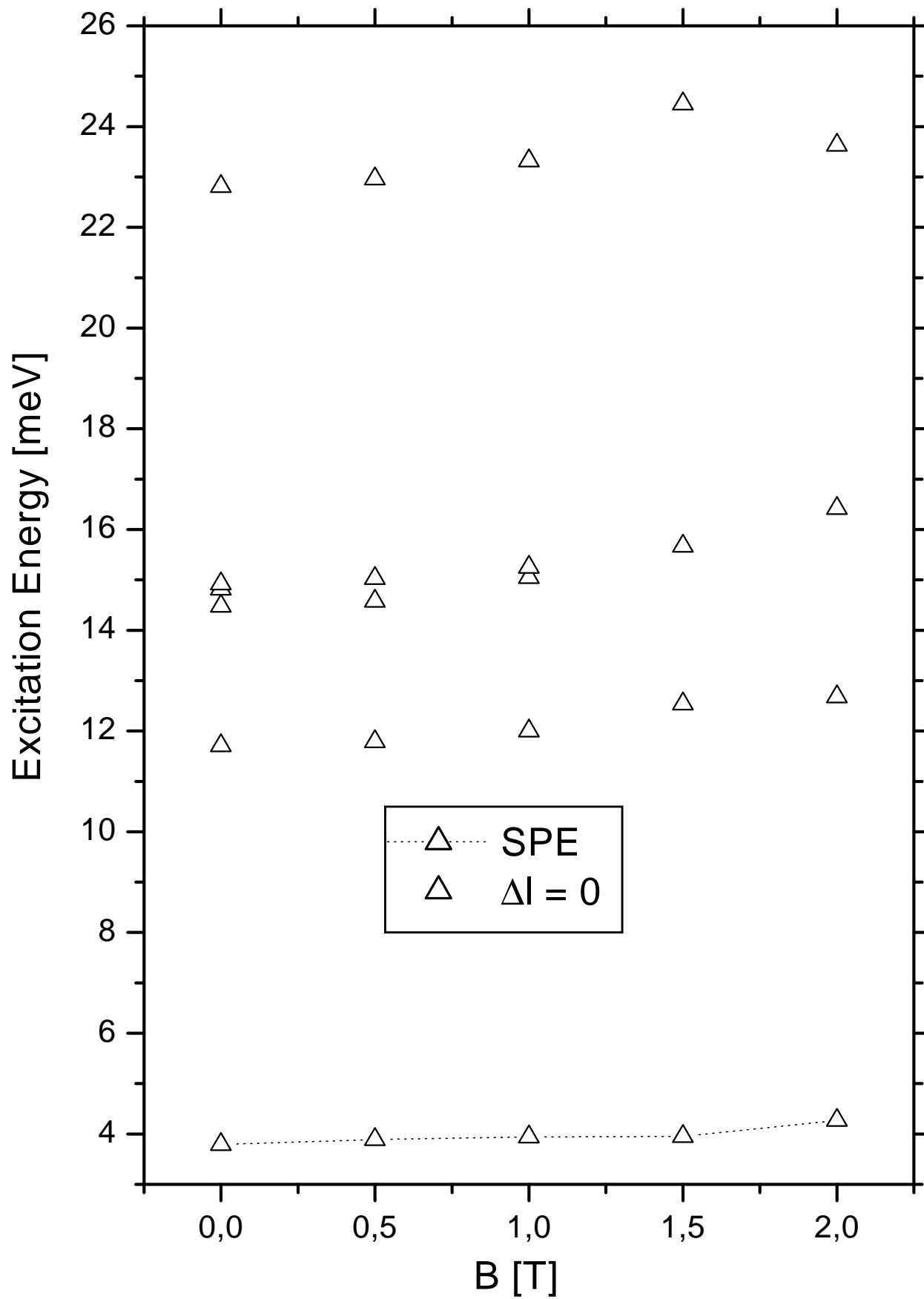


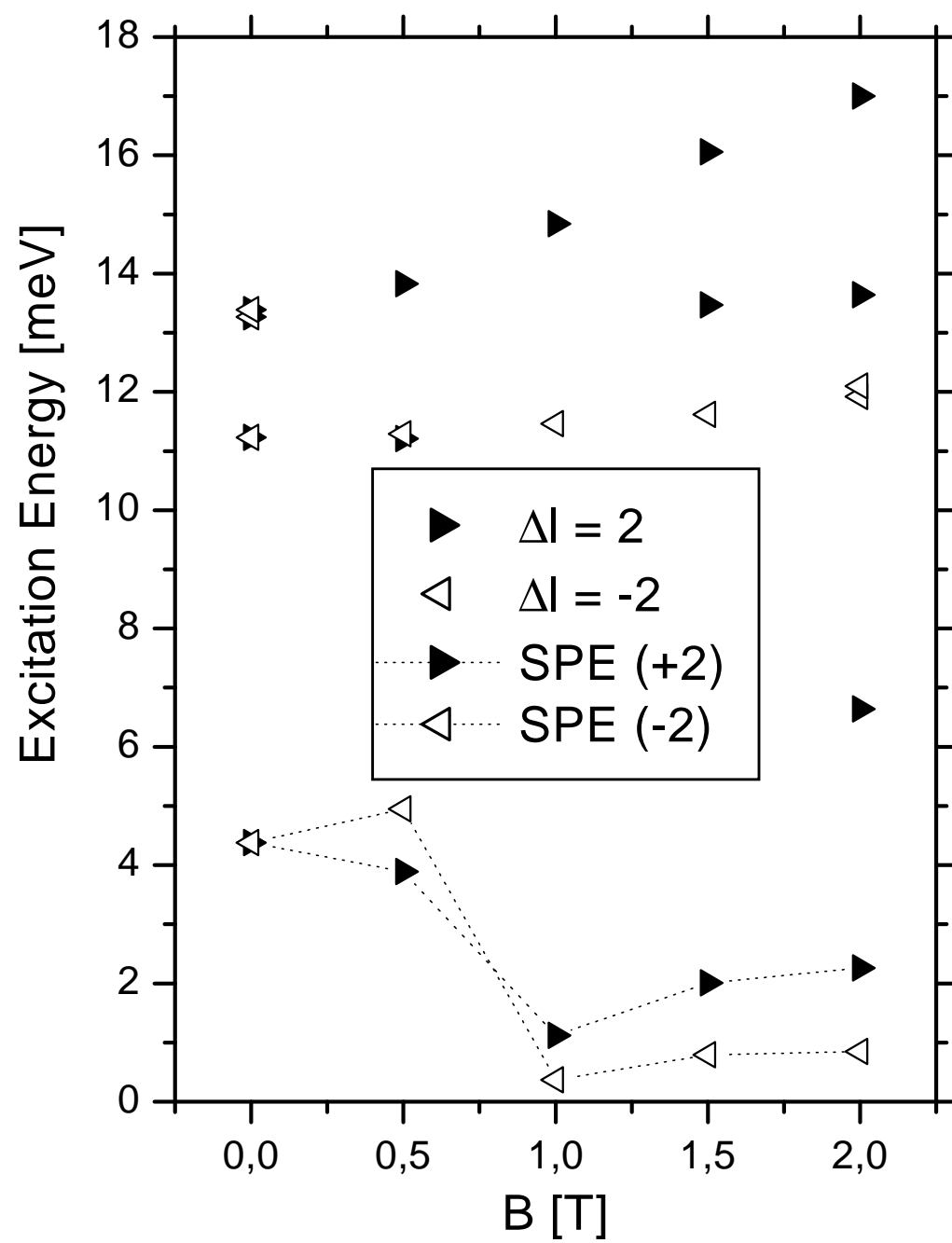
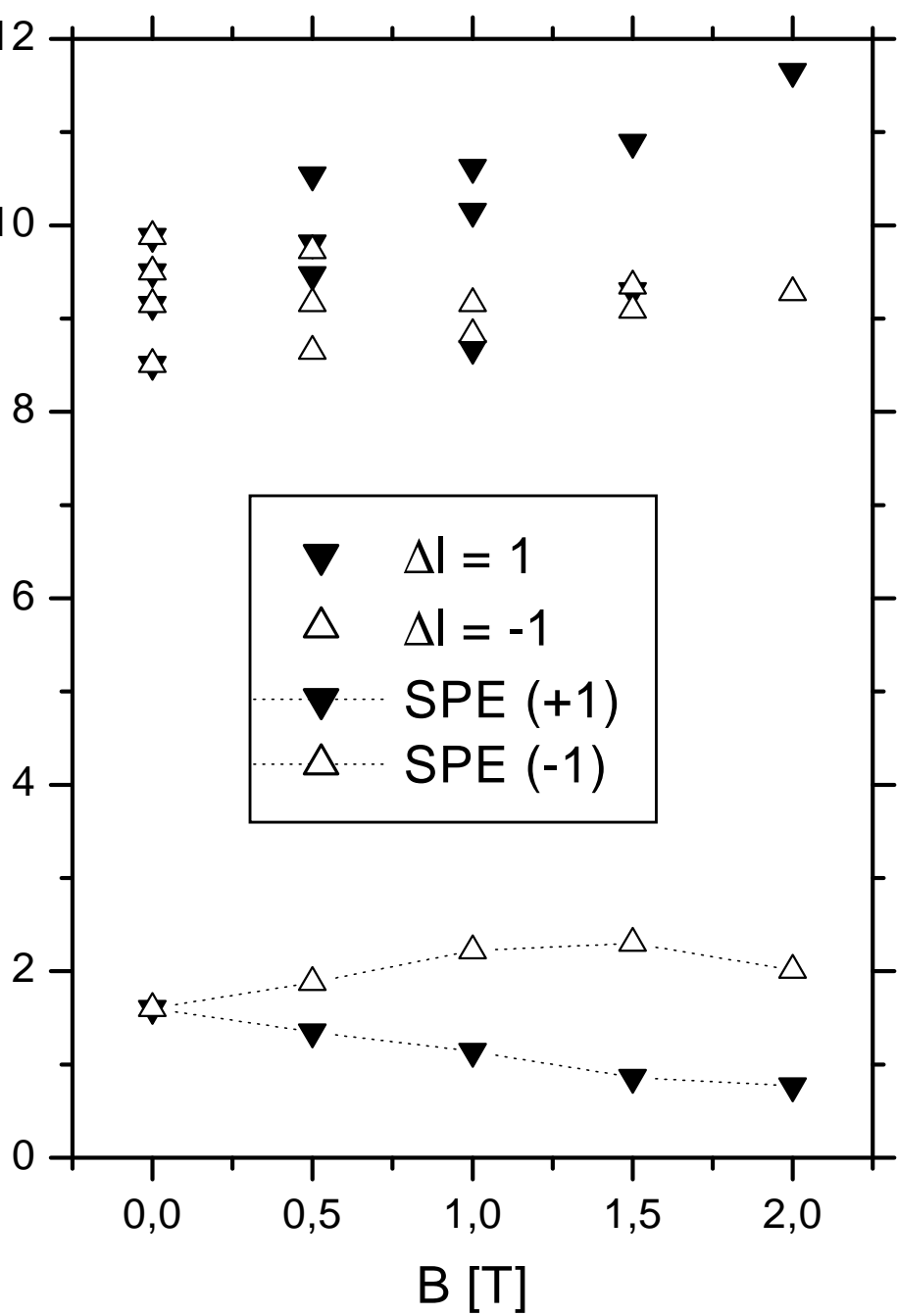
Raman Scattering (SDE)

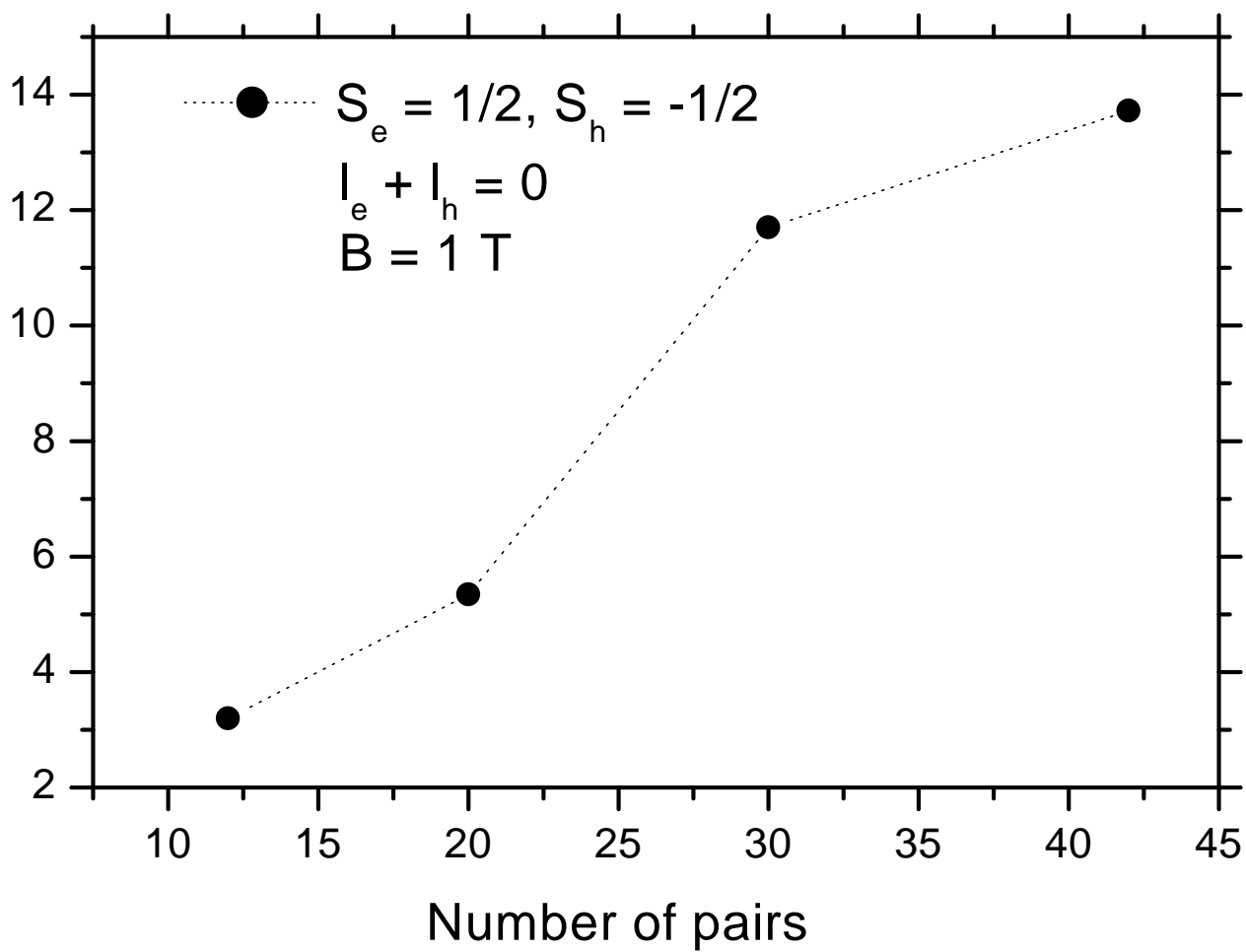
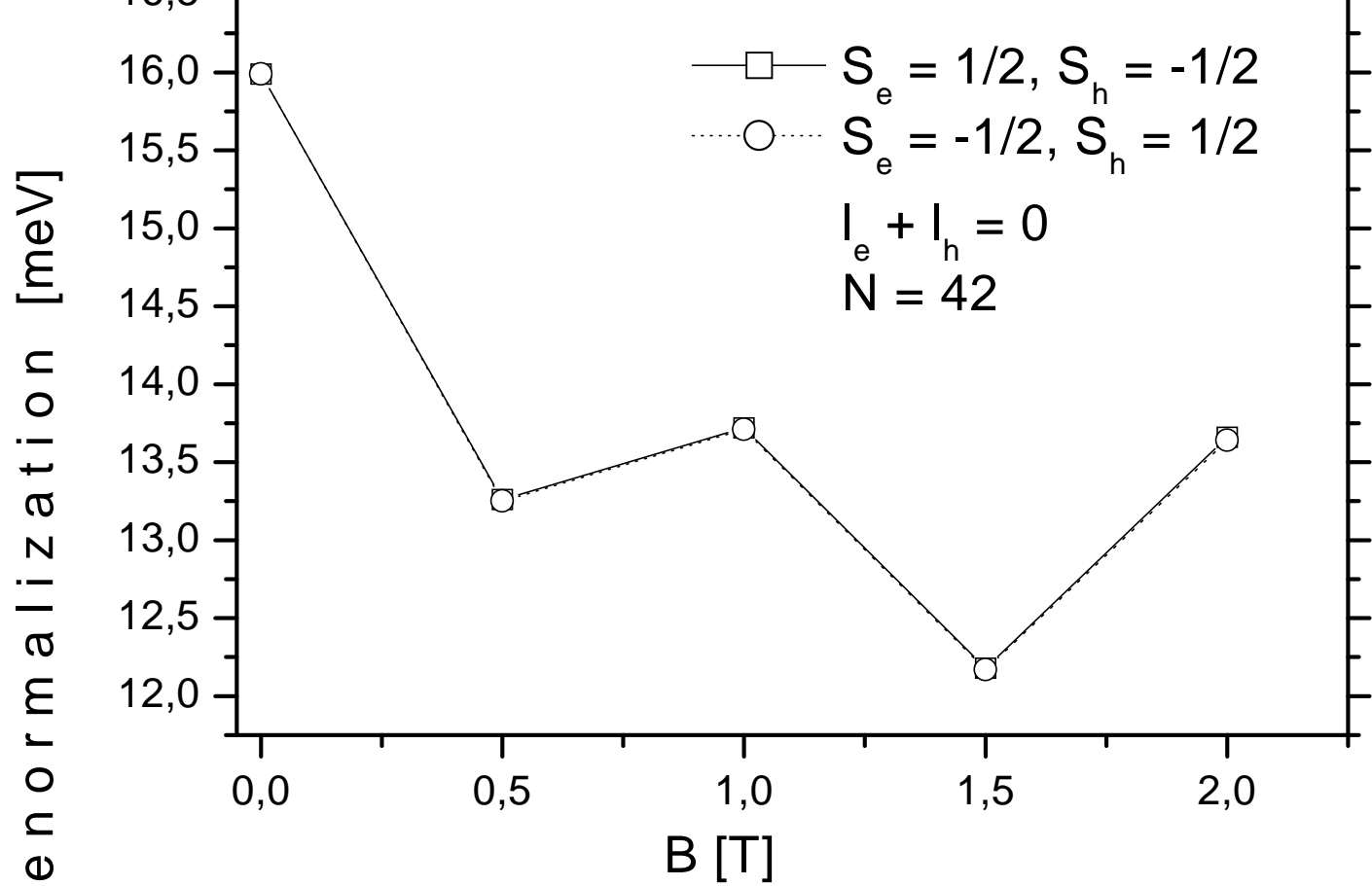


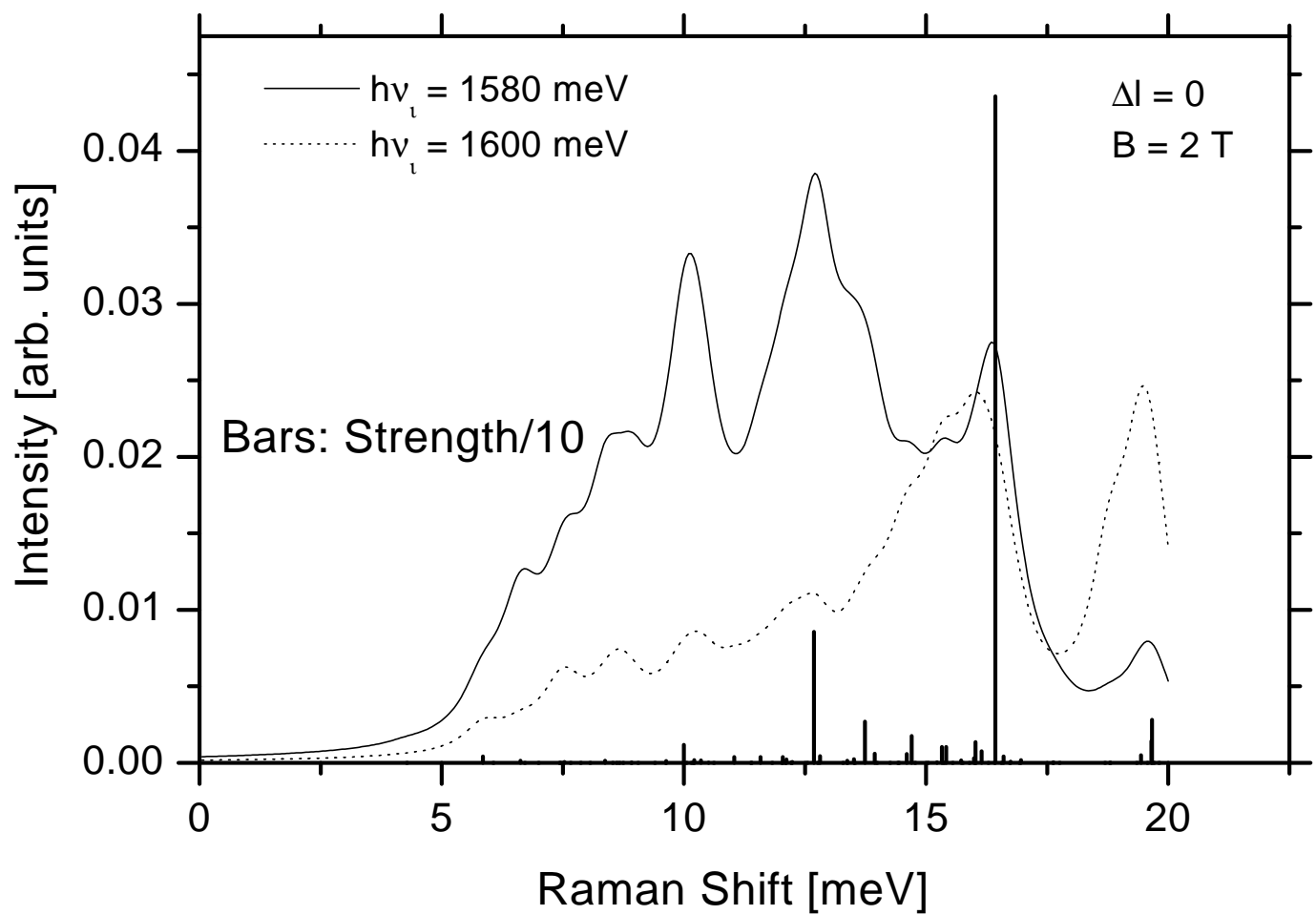
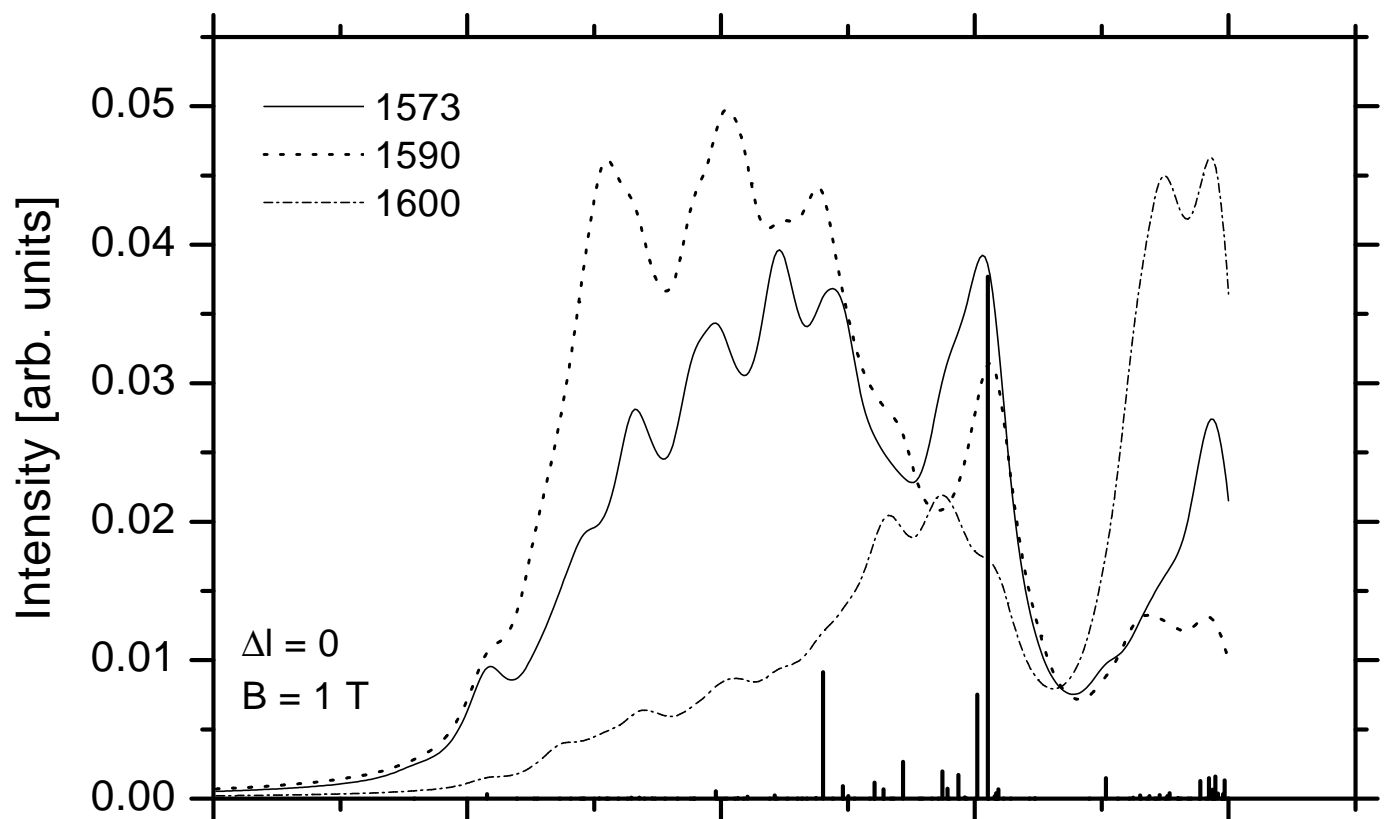


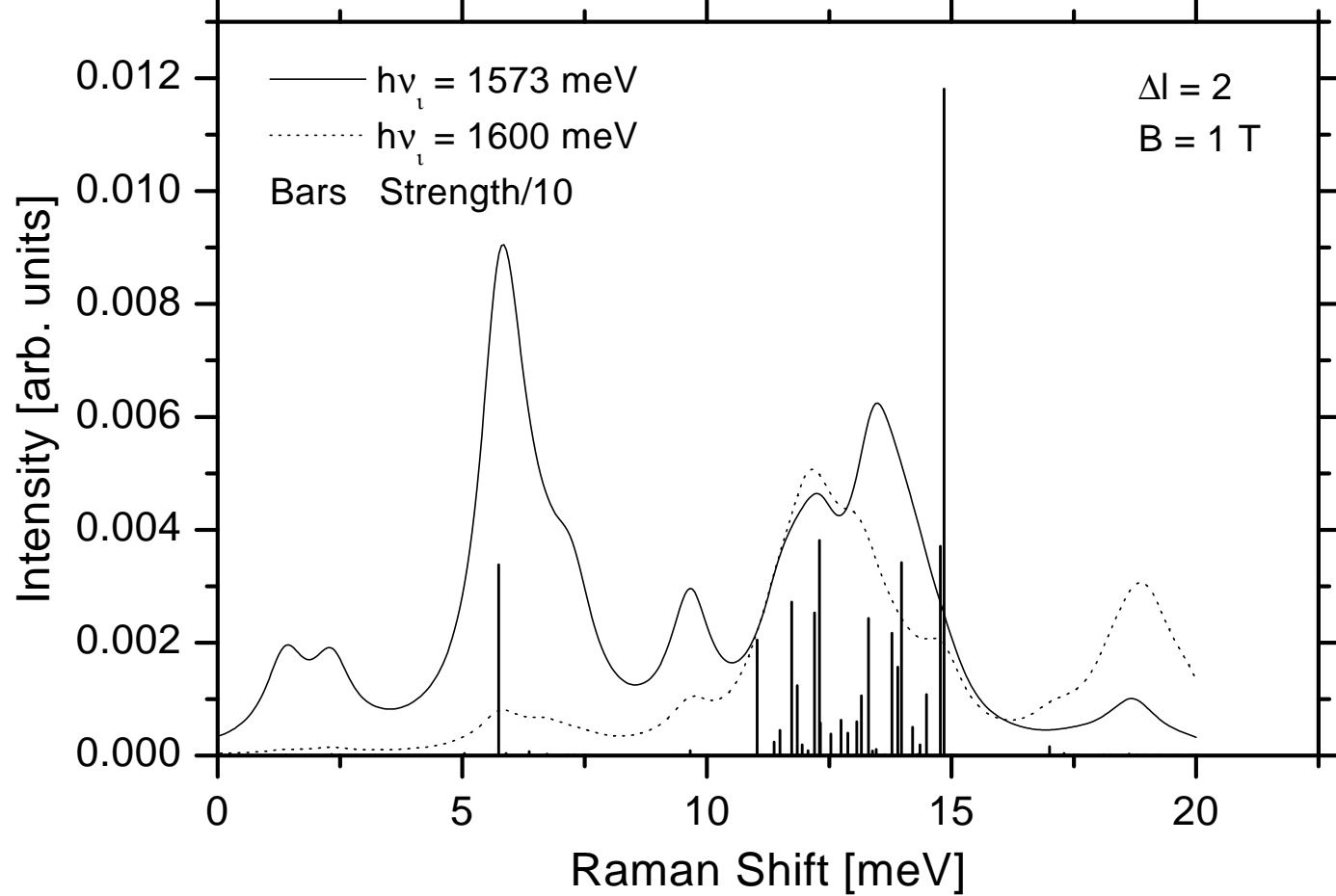
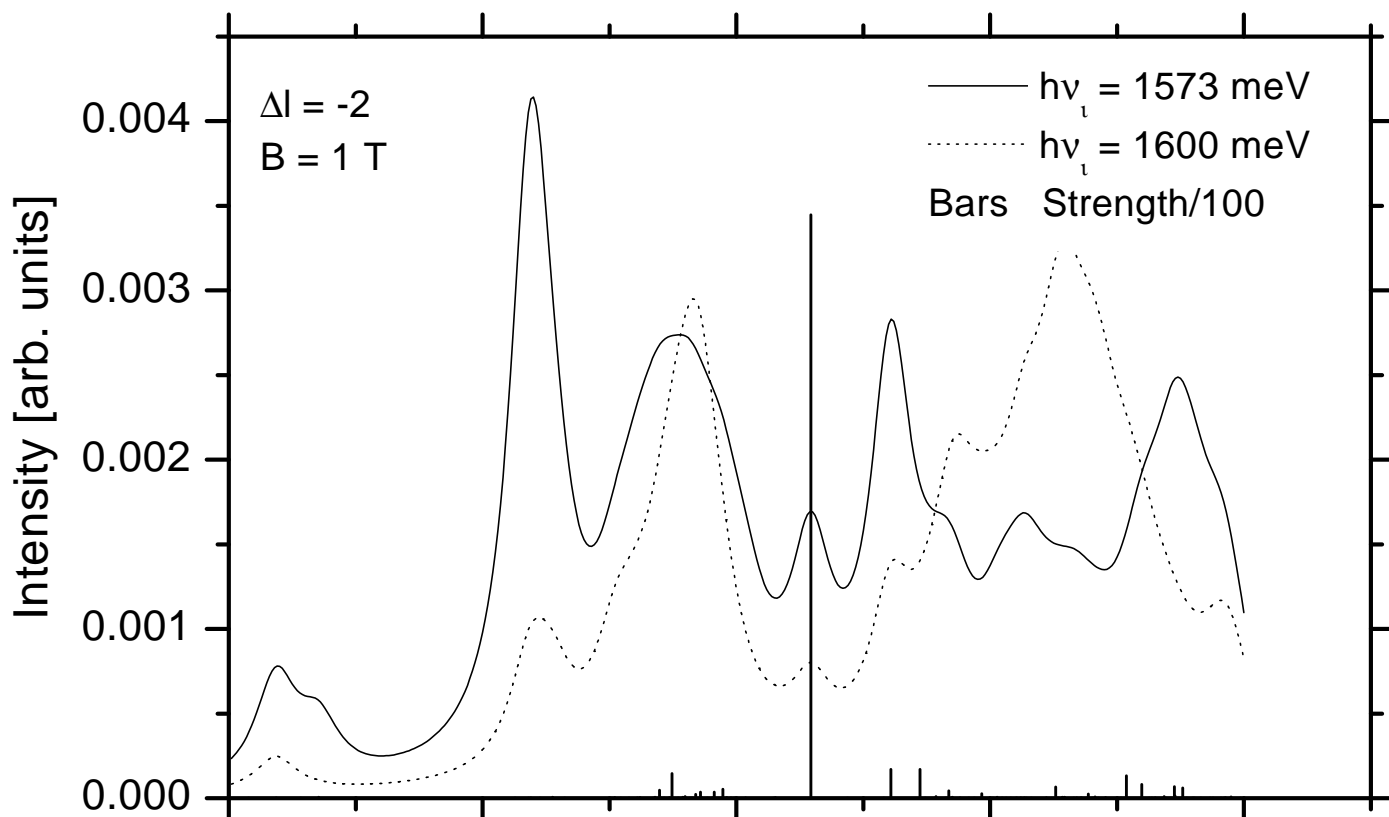












Orthogonal polarization

